From modeling to control of a variable stiffness device based on a cable-driven tensegrity mechanism

Quentin Boehler, Salih Abdelaziz, Marc Vedrines, Philippe Poignet, Pierre Renaud

HAL Id: lirmm-01370419

https://hal-lirmm.ccsd.cnrs.fr/lirmm-01370419

Submitted on 20 Sep 2018

HAL is a multi-disciplinary open access archive for the deposit and dissemination of scientific research documents, whether they are published or not. The documents may come from teaching and research institutions in France or abroad, or from public or private research centers.

L'archive ouverte pluridisciplinaire **HAL**, est destinée au dépôt et à la diffusion de documents scientifiques de niveau recherche, publiés ou non, émanant des établissements d'enseignement et de recherche français ou étrangers, des laboratoires publics ou privés.

CrossMark

From modeling to control of a variable stiffness device based on a cable-driven tensegrity mechanism

Quentin Boehler [a,*], Salih Abdelaziz [b], Marc Vedrines [a], Philippe Poignet [b], Pierre Renaud [a]

[a] ICube, University of Strasbourg, CNRS, 1 place de l'Hôpital, 67000 Strasbourg, France
[b] LIRMM, University of Montpellier, CNRS, 161 rue Ada, 34090 Montpellier, France

A B S T R A C T

Cable-driven tensegrity mechanisms are now considered for various applications in which their reconfiguration capacities are required together with their inherent lightness. Moreover, they can exhibit interesting variable stiffness capacities through the modification of their level of prestress when composed of deformable cables. Control schemes that deal with both reconfiguration and stiffness variation have however not been developed in the literature yet.

This paper presents two control strategies for that purpose to transform a cable-driven tensegrity mechanism into a variable stiffness device. The mechanism is a planar tensegrity mechanism allowing us to control an angular position and the associated stiffness. Relying on the properties of the mechanism models, the proposed control strategies allow a modulation of the stiffness or of its first time derivative. The interest of both propositions is outlined and an experimental investigation of their characteristics is performed. Encouraging results are obtained in terms of reconfiguration capabilities and stiffness variation.

© 2016 International Federation for the Promotion of Mechanism and Machine Science Published by Elsevier Ltd. All rights reserved.

1. Introduction

1.1. State of the art

Tensegrity mechanisms are a class of self-stressed systems defined as a set of compressed bars in a set of tensioned elements [1] that can be either rigid or elastic cables. Large reconfiguration of such mechanisms can be obtained through the actuation of the bars or the cables. Moreover, high dynamics are usually achievable thanks to their parallel architecture and their structural lightness [1]. For these reasons, the use of tensegrity mechanisms has appeared of great interest in various applications ranging from mobile robotics [2–4], to manipulators [5,6] and deployable systems [7,8].

Besides, the stiffness of a tensegrity structure composed of elastic cables can be drastically modified along specific directions through a modification of the level of prestress within the cables [9]. This interesting property has been successfully exploited in [10] to design a variable stiffness component. Such use is motivated by the interesting results obtained with

---

* Corresponding author.
  E-mail address: q.boehler@unistra.fr- (Q. Boehler).

similar strategies in the context of variable stiffness actuators [11]. In this case, the stiffness comes from the deformation of a compliant part within the system, such as a spring or a tendon, and a modification of its level of prestress provides a variation of the internal passive stiffness of the mechanism.

Fully exploiting tensegrity mechanisms should allow the modification of the position and the stiffness with a single robotic system. Such capabilities have however not yet been exploited, due to the absence of adequate control strategy. The goal of the paper is therefore to develop such control scheme.

The control of cable-driven tensegrity mechanisms is tedious as cables need to be constantly tensioned. They indeed impose *unidirectional* constraints, contrary to classical parallel manipulators in which the kinematic redundancy can be managed through *bidirectional* constraints [12]. Some prior works have been focused on the configuration control of cable-driven tensegrity mechanisms. For applications in mobile robotics such as [13], the main concern is the generation of a gait pattern to move the system center of mass regardless of an accurate configuration tracking. Positive tensions are then ensured by bounding the actuators range of motion. In more complex mechanisms as the ones assessed in [4,14], this constraint is managed in a quasi-static state using the equilibrium matrix of the system. This aims at finding the actuator states compatible with admissible cable tensions for a stable target configuration. Interestingly, similar constraints are encountered when considering cable-driven robots. A platform is then connected to the ground by cables whose lengths are coordinately modified to control the platform pose. In this case, the problem of unidirectional constraints is generally solved using tension distribution algorithms [15]. Until now, such algorithms aimed at finding the most suitable cable tensions within an admissible positive range [16,17]. The only goal is then to avoid negative tensions in the cables by discarding the non-compatible actuators state. A modulation of tension within its compatible range is of interest in our context, in order to bring a stiffness variation to the system.

1.2. Contributions

Our objective is to introduce control strategies for position and passive stiffness control of tensegrity mechanisms. To do so, the case study of a planar cable-driven tensegrity mechanism is used. Such a mechanism is interesting for the achievable control of an angular position and the associated stiffness. Its modeling properties are identified and control schemes built from them.

Our contributions include the development of two adapted control strategies that are shown to fulfill our objectives, while being complementary. Both are dealing with the system redundancy, and they provide a modulation of the system stiffness or of its first time derivative. The first strategy exploits a tension distribution algorithm inspired from those implemented in cable-driven robots. The second one proposes a novel velocity distribution algorithm. An implementation and an evaluation of these developments are achieved through the control of the considered planar cable-driven tensegrity mechanism. Their characteristics and their relative performances are experimentally assessed and discussed.

The modeling of the considered mechanism is first developed in Section 2. The two control strategies are then presented in Section 3. An experimental validation of our approach on a dedicated setup is presented in Section 4 and results are discussed in Section 5. Conclusions and perspectives in terms of generalization are finally given in Section 6.

2. System modeling

2.1. Description of the mechanism

The tensegrity mechanism under study is depicted in Fig. 1. It is a planar mechanism composed of three moving bars and one bar linked to the base, all of equal length L. The four bars are considered as perfectly rigid and articulated by four pin joints in A, B, C and D. The obtained parallelogram linkage is actuated by two inelastic cables attached in C and D, passing respectively through A and B. It is a class-2 tensegrity mechanism [18] as the bars are compressed by the two tensioned actuated cables. It is considered as a 1-DOF mechanism whose end-effector is the bar BC, and its configuration is described by the angle θ. Such a mechanism can for instance be integrated in medical applications [19,20]. Two linear springs of stiffness k are integrated along each cable to bring compliance to the linkage when the cables are tensioned. The end-effector angular stiffness is denoted K_θ. The distances AC and BD are respectively denoted l_1 and l_2 and can be computed as

$$\begin{cases} l_1 = 2L \cos(\theta/2) \\ l_2 = 2L \sin(\theta/2) \end{cases} \tag{1}$$

The two lengths will be noted with the compact form $\mathbf{l} = [l_1, l_2]^T$. Cables are actuated by two actuators whose angular positions are described by the vector $\boldsymbol{\alpha} = [\alpha_1, \alpha_2]^T$ (Fig. 1). Pulleys of radius R are mounted on the actuators so that $\mathbf{q} = [q_1, q_2]^T = -R\boldsymbol{\alpha}$ describes the cable displacement. The springs are the only compliant elements in the system, structural elements and actuators being considered rigid. They reach their free length for $\mathbf{q} = \mathbf{l}$ as each length $q_i, i \in [1, 2]$ is measured from the cable take-off point on the actuated pulley to the actuator-side end of the i-th spring. In the following, $\mathbf{q}$ is designated as the *articular variables*, and the configuration of the system is represented by the *operational variable* θ.
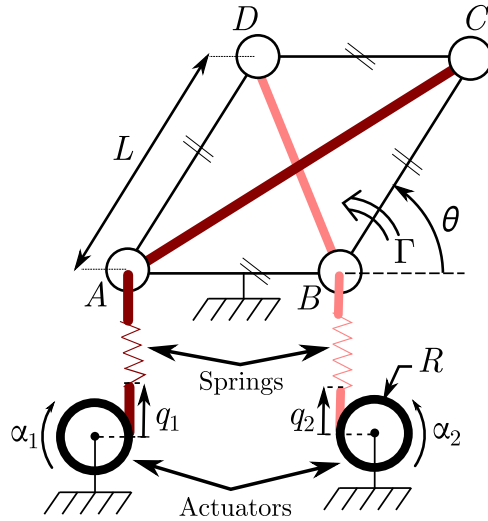
Fig. 1. Cable-driven planar tensegrity mechanism.

2.2. Kinematic and static modeling

As the tensegrity mechanism is composed of deformable springs, it is submitted to self-equilibrium and kinematic constraints [21]. Kinematic modeling is used, neglecting here the system dynamics. The elements of the tensegrity structure are indeed lightweight, so their dynamic behavior can often be neglected in the modeling. The impact of this modeling approach will be discussed from the experimental results. The statics of the system are then described by the equation

$$L \sin(\theta/2)F_1 - L \cos(\theta/2)F_2 = \Gamma \tag{2}$$

where $\mathbf{F} = [F_1, F_2]^T$ are the cable tensions and Γ is the torque generated by the cables on the output bar BC (see Fig. 1). The self-equilibrium of the system is reached when $\Gamma = 0$, which means that F_1 and F_2 are equilibrating the end-effector in the configuration θ.

Developing (2) for $\Gamma = 0$ together with (1), and given that $\mathbf{F} = k(\mathbf{l} - \mathbf{q})$, the so-called forward static model can be obtained as

$$\theta = 2 \arctan(q_2/q_1) \tag{3}$$

It relates the articular variables to the operational one. Note that this model can also be obtained using a potential energy minimization, a common form-finding method [22] applicable for any tensegrity mechanism. Since the springs are the only compliant parts of the system they store the whole potential elastic energy. Eq. (2) can also be written as

$$\mathbf{WF} = \Gamma \tag{4}$$

with $\mathbf{W} = [L \sin(\theta/2), - L \cos(\theta/2)]$. This form clearly shows the redundancy of the system, *i.e.* that two tensions are used to generate a single torque on the end-effector. According to the principle of virtual works, the redundancy also appears in the differential kinematic model, which is derived from the static model expressed in (3) so that $\dot{\theta} = \mathbf{J}\dot{\mathbf{q}}$ with

$$\mathbf{J} = \left(\frac{-2q_2}{q_1^2 + q_2^2} \quad \frac{2q_1}{q_1^2 + q_2^2} \right) \tag{5}$$

showing that two articular velocities are used to generate one velocity of the end-effector.

2.3. Redundancy and stiffness through prestress

Because of the system redundancy, both $\mathbf{W}$ and $\mathbf{J}$ are rank-deficient, and their nullspaces respectively contain the set of cable tensions, and the set of articular velocities that ensure the system equilibrium. In other words, a given configuration can be reached for several levels of prestress, and different articular velocities. The stiffness in each configuration can besides be computed as [22]

$$K_\theta = - \frac{\partial \Gamma}{\partial \theta} \tag{6}$$

The stability of the static equilibrium formulated with (2) is ensured when the stiffness K_θ is positive [22]. In the following, only positive stiffness configurations are considered, so that the equilibrium is always stable. Eq. (6) can be

combined with (2) to express K_θ according to the cable tensions as

$$K_\theta = -\frac{L}{2}(\cos(\theta/2)F_1 + \sin(\theta/2)F_2) + kL^2 \tag{7}$$

where F_1 and F_2 are chosen within the nullspace of **W** to ensure that $\Gamma = 0$. Interestingly, this equation shows that variations of prestress and stiffness K_θ are related. In a similar way, the articular velocities are related to the first time derivative of the stiffness, that will be designated as *stiffness derivative* in the following of the paper. It can be computed as the first derivative of (7) so that

$$\dot{K}_\theta = \frac{kL}{2}(\cos(\theta/2)\dot{q}_1 + \sin(\theta/2)\dot{q}_2) \tag{8}$$

where $\dot{q}_1$ and $\dot{q}_2$ are chosen within the nullspace of **J** to ensure that $\dot\theta = 0$. This non-usual notion of *stiffness derivative* is indeed of interest. It is a relevant property for an end-user who aims at modifying the system stiffness regardless of a targeted value. In applications involving for instance variable stiffness devices in interaction with a user, this latter is indeed sensitive to a stiffness variation rate rather than to the stiffness value. In that case, the stiffness value is not relevant for the user, and the specification of a stiffness variation within a given amount of time, *i.e.* a variation rate, can thus be preferred. A modulation of K_θ or $\dot{K}_\theta$ is thus of interest, depending on whether one aims at reaching a desired value of stiffness or wants an evolution of the stiffness along the time.

Finally, the kinematic redundancy is here represented by a physical property of the system, namely its stiffness. Eqs. (7) and (8) are used to modulate either K_θ or $\dot{K}_\theta$ through two control strategies that are developed in the following section.

3. Control strategies

Our objective is to control the configuration together with the stiffness or the stiffness derivative of the system. For this purpose, we take profit from the system redundancy. As shown in Section 2, the modulation of the stiffness or its derivative is closely related to the choice of adapted tensions or articular velocities within the nullspaces of **W** or **J** respectively. For this reason, the proposed strategies implement either a tension or a velocity distribution algorithm. Moreover, these algorithms have to ensure that each cable tension remains in a bounded positive interval $[F_{min}, F_{max}]$ all along the reconfiguration, with F_{min} and F_{max} respectively the minimum and maximum admissible tension. In the following, we will use the vectors $\mathbf{F}_{min} = [F_{min}, F_{min}]^T$ and $\mathbf{F}_{max} = [F_{max}, F_{max}]^T$ to describe admissible tensions for the two cables.

3.1. Force control strategy

3.1.1. Tension distribution
The structure of the first control strategy is adapted from [23] and depicted in Fig. 2(a). An external loop controls the current configuration θ_m from its reference θ^* using a position controller that generates a signal Γ_v homogeneous to a torque. This signal is used as an input to the tension distribution algorithm that generates the reference tensions $\mathbf{F}^*$ to be followed by the system. This algorithm solves

$$\mathbf{W}\mathbf{F}^* = \Gamma_v, \quad \text{subjected to } \mathbf{F}_{min} \leq \mathbf{F}^* \leq \mathbf{F}_{max} \tag{9}$$

where the vector inequalities are element-wise. The solution of (9) is of the form [15]

$$\mathbf{F}^* = \mathbf{W}^+\Gamma_v + \mathbf{N}_W\lambda_1 \tag{10}$$

where $\mathbf{N_W} = [-L\cos(\theta/2), -L\sin(\theta/2)]^T$ is a basis of **W** nullspace, $\mathbf{W}^+$ denotes the Moore–Penrose pseudoinverse of **W**, and λ_1 a scalar to be chosen so that the inequality in (9) is satisfied. The solution to (9) is indeed bounded and can be expressed as
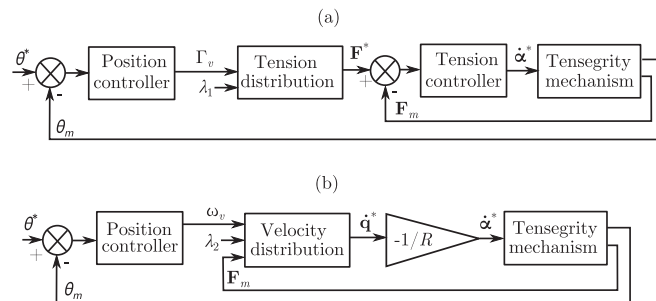
(a)

(b)

Fig. 2. Schemes of the force control strategy (a) and velocity control strategy (b).

$$\mathbf{F_{min}} - \mathbf{W}^+ \varGamma_v \leq \mathbf{N_W} \lambda_1 \leq \mathbf{F_{max}} - \mathbf{W}^+ \varGamma_v \tag{11}$$

The existence of a solution to (9) depends on the value of $\varGamma_v$ that corresponds to a torque to be generated on the end-effector by the two cables. Besides, each cable tension should remain in the bounded interval [F_{min}, F_{max}]. Consequently, (9) does not admit a valid solution (10) when $\varGamma_v$ can only be generated by tensions that does not belong to this interval. The feasibility of $\varGamma_v$ is first verified. We then propose to saturate it accordingly using the approach of [24] to ensure the existence of a solution set. The set $\varLambda_1 = \{\lambda_1 | \lambda_{min} \leq \lambda_1 \leq \lambda_{max}\}$ can then be computed from (11), with λ_{min} and λ_{max} the minimum and maximum value of λ_1 respectively.

The tension distribution algorithm is classically used to provide a single feasible solution to (10) among the infinite number of solutions in $\varLambda_1$ [15]. The scalar λ_1 can for instance be chosen as the center of gravity of $\varLambda_1$, which has been proved to be continuous along continuous trajectories [25]. As $\varLambda_1$ is here a 1-dimensional manifold, its center of gravity corresponds to a mid-range point that is computed as $(\lambda_{max} + \lambda_{min})/2$. A physical understanding of this choice is that the level of prestress is then as far away as possible from its upper and lower bounds. Interestingly, the second term of (10) corresponds to the level of prestress within the system. The modulation of λ_1 within $\varLambda_1$ has a direct impact on the stiffness regardless of the system configuration. This remark is here at the base of the stiffness control with the tension distribution algorithm, which is therefore here exploited in an original way.

Once the proper reference $\mathbf{F}^*$ is computed, an inner loop is implemented for the control of the current tensions $\mathbf{F}_m$ using the tension controller to feed the actuators with the corresponding desired actuator velocities $\dot{\alpha}^*$.

3.1.2. Modulation of stiffness
Around an equilibrium configuration, $\varGamma_v = 0$ and (10) becomes

$$\mathbf{F}^* = \mathbf{N_W} \lambda_1 \tag{12}$$

Assuming that the desired tensions are reached, combination of (12) and (7) gives the following expression of the stiffness:

$$K_\theta = \frac{L^2}{2}(\lambda_1 + 2k) \tag{13}$$

This means that K_θ can be explicitly modulated through λ_1. One can finally notice that choosing λ_1 as the center of gravity in $\varLambda_1$ leads the system to be at its mean reachable stiffness all along its reconfiguration.

3.2. Velocity control strategy

3.2.1. Velocity distribution
The structure of the second control scheme is depicted in Fig. 2(b). The external loop is identical to the previous one but instead of a signal homogeneous to a torque, it generates a signal ω_v homogeneous to an angular velocity of the end-effector. This signal feeds a so-called velocity distribution algorithm that directly generates the appropriate desired articular velocities $\dot{\mathbf{q}}^*$. The tension controller is hereby suppressed. The velocity distribution algorithm solves the following constrained linear system of equations:

$$\mathbf{J}\dot{\mathbf{q}}^* = \omega_v, \quad \text{subjected to } \mathbf{F_{min}} \leq \mathbf{F} \leq \mathbf{F_{max}} \tag{14}$$

whose solution is of the form

$$\dot{\mathbf{q}}^* = \mathbf{J}^+ \omega_v + \mathbf{N_J} \lambda_2 \tag{15}$$

where $\mathbf{N_J} = [2q_1/(q_1^2 + q_2^2), 2q_2/(q_1^2 + q_2^2)]^T$ is a basis of $\mathbf{J}$ nullspace, $\mathbf{J}^+$ denotes the Moore–Penrose pseudoinverse of $\mathbf{J}$, and λ_2 a scalar to be chosen so that the inequality in (14) is satisfied. This constraint is formulated on the cable tensions $\mathbf{F}$, whereas the velocity distribution algorithm deals with velocities. The two quantities are linked through the elastic characteristic of the springs, so the constraints of (14) can be reformulated with respect to the articular velocities as given in Appendix A.

The method used to compute the set $\varLambda_1$ can also be applied to compute the set $\varLambda_2$ that bounds the choice of λ_2. The second term in (15) corresponds to articular velocities that do not modify the system configuration as it is chosen in the nullspace of the $\mathbf{J}$ matrix. Then using (8), one can modify $\dot{K}_\theta$ about an equilibrium configuration by modulating the choice of λ_2 in $\varLambda_2$.

3.2.2. Stiffness derivative modulation
An approach similar to the one described in Section 3.1.2 can be developed using the velocity distribution algorithm with $\omega_v = 0$ so that (15) becomes

$$\dot{\mathbf{q}}^* = \mathbf{N_J} \lambda_2 \tag{16}$$

Assuming that the desired velocities are reached, the combination of (16) and (8) gives the following stiffness derivative expression:
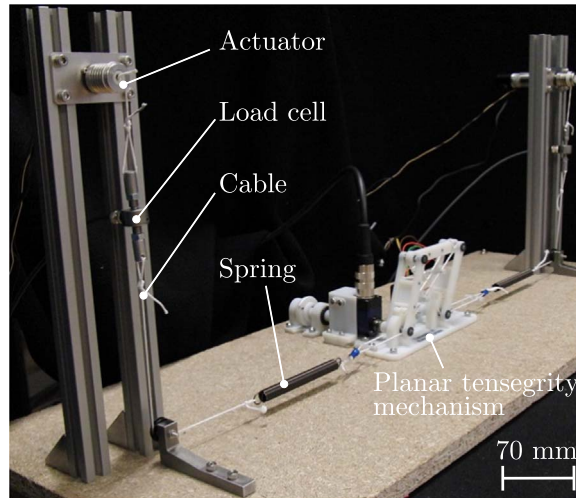
Fig. 3. General view of the experimental setup.

$$\dot{K}_\theta = \frac{kL}{\sqrt{q_1^2 + q_2^2}} \lambda_2$$

(17)

This means that $\dot{K}_\theta$ can be explicitly modulated through λ_2 using this strategy. Once again, this constitutes an interesting and original use of the velocity distribution algorithm to modify the stiffness derivative $\dot{K}_\theta$.

4. Experimental analysis

The control strategies allow the reconfiguration of the proposed mechanism. Moreover, the developed tension and velocity algorithms allow a stiffness, or a stiffness derivative control about an equilibrium configuration. This section aims at evaluating experimentally these strategies. To do so, the planar tensegrity mechanism in Fig. 1 is implemented with dimensions compatible with an application issued from medical robotics [26].

The evaluation is conducted by assessing separately the performance of the reconfiguration, the modulation of stiffness and the modulation of stiffness derivative.

4.1. Experimental setup

The experimental setup is depicted in Figs. 3 and 4. Two DC actuators (Harmonic Drive ® RH-5A) are used to drive the cables through pulleys. Standard linear springs of stiffness 2.70×10^{-1} N/mm $\pm$ 5% are integrated along the cables. Load cells (Scaime ® K1107, 50 N) are integrated between the springs and the actuators. A torquemeter (Fig. 4, Scaime ® DR1, 1 N m) is also integrated in one of the parallelogram joints (A, Fig. 1) to estimate the mechanism stiffness. An optical encoder (Fig. 4,
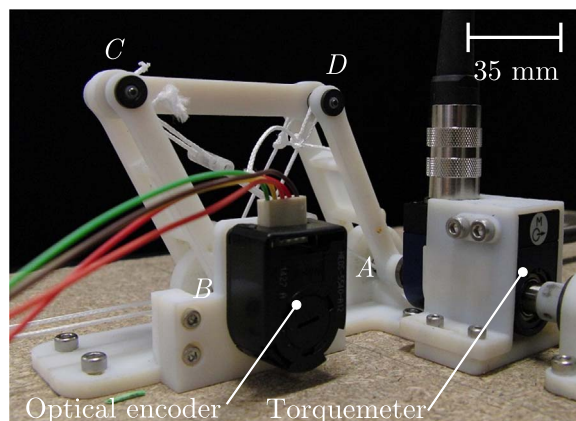

Fig. 4. Instrumentation of the cable-driven planar tensegrity mechanism.

HP ® HEDS-5540) is finally mounted on the revolute joint located in B (Fig. 1) to measure the current angle θ_m. These instruments ensure a measure of angle with an accuracy of 1.26×10^{-2} rad and a measure of torque with an accuracy of 1.00×10^{-3} N m.

The planar tensegrity mechanism is produced using additive manufacturing with polymer materials. Shafts, made out of brass and polymer bushings, are employed. For this setup, the bars length is chosen equal to $L = 70$ mm and the geometry is chosen so that the angular range of the angle θ is equal to $[\pi/4, \pi/2]$ rad. Two EPOS3 70/10 EtherCAT ® controllers are configured to control the actuators in velocity and acquire the different sensors signals on an EtherCAT ® fieldbus coupled to a real-time Linux system.

The structural parts can be considered rigid compared to the springs thanks to their constitutive material and dimensions. In a similar way, we ensure that the actuators stiffness can be neglected thanks to the high gear ratio and their control.

The position and tension controllers for both strategies are implemented with proportional gains. Their values have been experimentally tuned so that the position controller gains are respectively $K_{p1} = 4.00$ N m/rad and $K_{p2} = 1.40$ s^{-1}, and the tension controller gain is $K_t = 3.00 \times 10^2$ rad s^{-1} N^{-1}. The impact of this choice on the behavior of the system is discussed in Section 5.

4.2. Reconfiguration experiment

First, a trajectory tracking experiment is performed to assess the reconfiguration capacity of the system, and the impact of the tensions bounds on the system behavior. In these experiments, λ_1 and λ_2 are chosen as the center of gravity of Λ_1 and Λ_2 respectively. Two trajectories are tracked with both strategies in order to assess the controller performances for different dynamics.

4.2.1. Low dynamics trajectory

As a first experiment, the chosen trajectory is a third-order curve that goes from $\theta_* = \pi/2$ rad to $\pi/4$ rad during the first 30 s with constant bounds on **F**, namely 4 N and 10 N. Between 35 s and 38 s, the upper bound is linearly increased from 10 N to 20 N for $\theta_* = \pi/4$ rad.

The results are depicted in Fig. 5(a). At $\theta_* = \pi/2$ rad, the tensions in the cables are equal due to the symmetrical arrangement. Moreover, they are equal to $(F_{min} + F_{max})/2 = 7$ N, the center of gravity of the feasible tensions.

The trajectory is accurately tracked with both strategies, with a mean tracking error of 1.75×10^{-2} rad and 1.57×10^{-2} rad respectively while maintaining the tensions in the prescribed range. The static error remains below the encoder resolution. Finally, when F_{max} is increased from 10 N to 20 N, the cable tensions continuously adapt to the new bounds while the configuration remains identical.

In order to assess the robustness of the distribution algorithms to modeling errors, the tracking is repeated with 20% error on k and L values. This constitutes very large variations regarding the usual knowledge on such parameters. The differences in the resulting tracking and static errors with respect to the experiments where nominal values of k and L are considered remain below the encoder resolution. Both strategies thus seems pretty robust to modeling errors under these experimental conditions.

4.2.2. High dynamics trajectory

A second trajectory with higher dynamics is being tracked. The angle θ_* is varied from $\pi/2$ rad to $\pi/4$ rad in 5 s, which means that the velocity is multiplied by 6, and the acceleration by 36. The experimental conditions are identical except the modification of the tensions bounds at the end of the tracking.

As depicted in Fig. 5(b), the performance is decreased, with a mean tracking error of 6.28×10^{-2} rad and 8.73×10^{-2} rad respectively and significant errors on the internal loop for the first strategy. The system however remains stable and the static error remains below the encoder resolution. Moreover, the tension bounds are still respected for this case study and the implemented distribution algorithms are effective for these experimental conditions.

These first results show the ability to track a trajectory with both control strategies while respecting the tension bounds, even with significant errors on k and L values. A slow dynamic trajectory can be accurately tracked. High dynamics tracking exhibits higher errors due to the simplicity of the implemented controllers, but stability and zero static error are still ensured with both strategies. The possible tension modulation for a fixed configuration is also demonstrated, here as a consequence of the tension bounds modification in the first experiment.

4.3. Modulation of stiffness

As the proposed strategies allow an accurate reconfiguration of the system, the achievable modulations of stiffness are experimentally evaluated along the angular range of motion.

First, the theoretical minimum, maximum and mean stiffnesses of the system, respectively denoted K_θ^{min}, K_θ^{max} and K_θ^{moy}, are computed using (7) for the tension bounds [4,20] N. The angular range is then discretized in 10 angles between $\pi/4$ rad and $\pi/2$ rad. For each angle, the stiffness is experimentally evaluated for the three stiffness levels. To do so, the mechanism is positioned around the desired equilibrium configuration θ_* using the force control strategy, and λ_1 is chosen to reach the desired stiffness (see (13)). A deflection $\delta\theta$ from the equilibrium configuration θ_* is then applied through a loading system
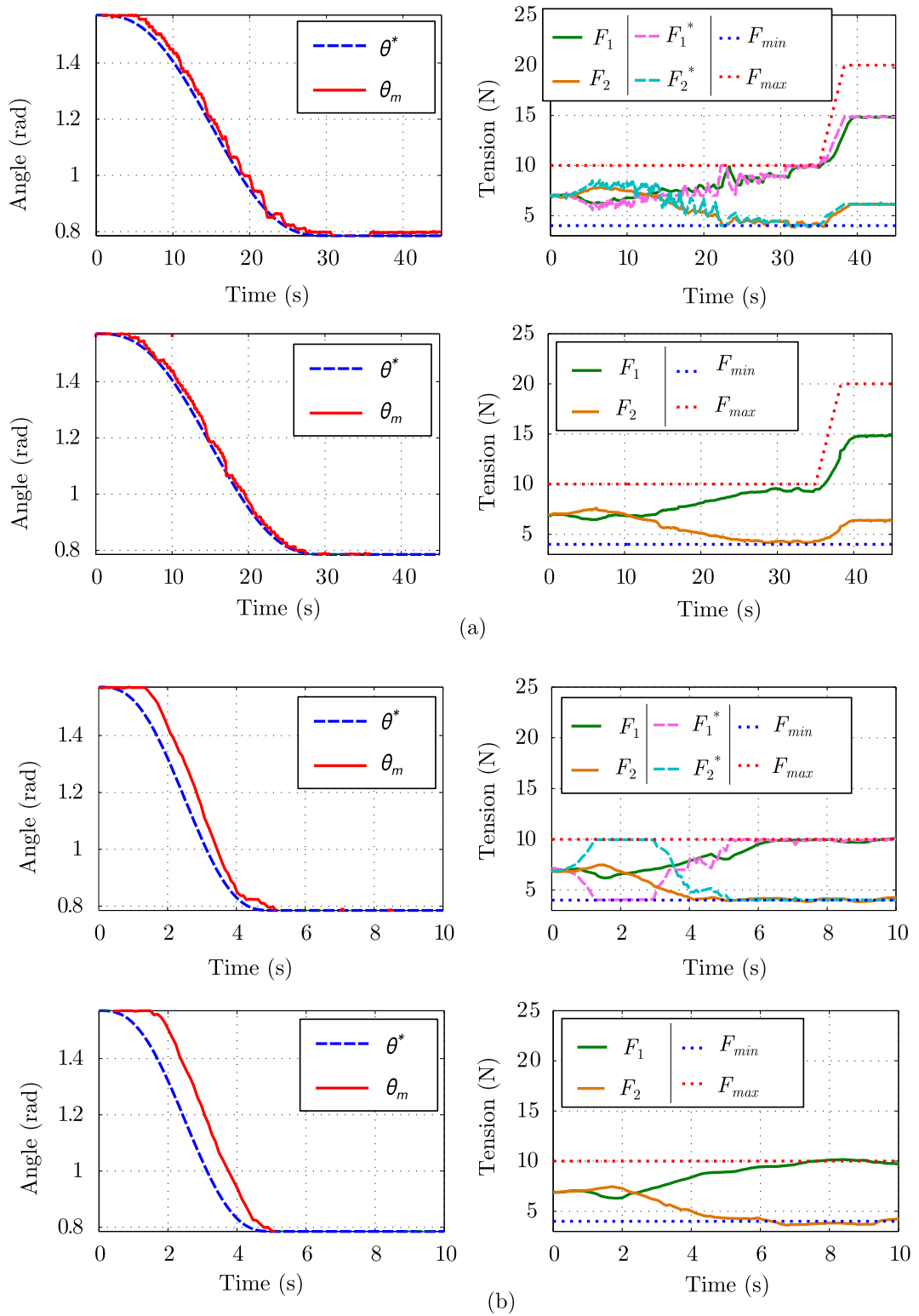
Fig. 5. Trajectory tracking: (a) for a low speed trajectory and (b) for a high speed trajectory. Up using the force control strategy and bottom using the velocity control strategy. The measured angle θ_m and its reference θ^* are on the left, the cable tensions and their bounds are on the right for each experiment.
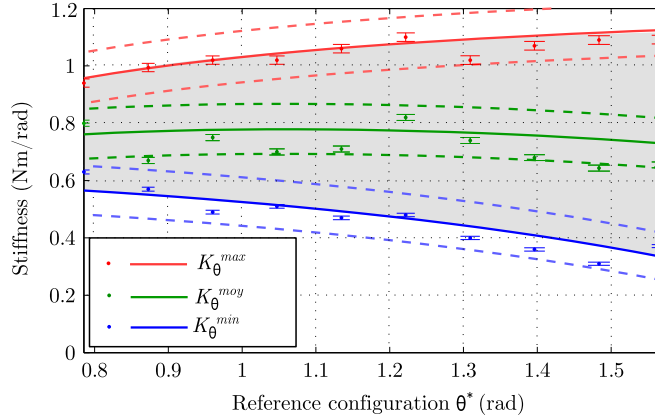
Fig. 6. Modulation of stiffness. The nominal predicted values are represented by plain lines and the experimental data by points. Dotted lines represent the modeling error dispersion around the nominal values, and the measurement uncertainties are represented by error bars. Gray area represents the nominal achievable range of stiffness.

coupled to the torquemeter that measures the resulting torque δT (Figs. 1 and 4) while the system is in open loop. The angular stiffness can then be estimated with the relationship $\delta T/\delta\theta$. Note that the angular deflection of the actuator output shaft remains below the encoder resolution during the experiments on the considered tension range, which confirm the validity of the modeling.

The experimental results and their comparison to the simulations are depicted in Fig. 6. The maximum stiffness variation range can be obtained for $\theta^* = \pi/2$ rad. This range is shrinking when the system configuration goes toward $\pi/4$ rad. The stiffness variation capacity of the system using this strategy is experimentally confirmed and accurately matches the simulations with a mean error of 7% (standard deviation of 5% and maximum of 20%). Model errors and measurement uncertainties explain the observed disparities between model and experiment as depicted in Fig. 6.

4.4. Modulation of stiffness derivative

The stiffness derivative modulation is assessed in a second step. The maximum and minimum stiffness derivative $\dot{K}_\theta$ are theoretically determined for each configuration using (3) and (8) and the prescribed maximum output velocities of the actuators. The discretization of the angular range of motion described in Section 4.3 is considered to evaluate the modulation of $\dot{K}_\theta$.

Measurements are performed in four steps. First, the mechanism is set around a desired equilibrium configuration θ^* using the velocity control strategy. A deflection $\delta\theta$ is then applied and the resulting torque δT is measured with the torquemeter. Then λ_2 is set to reach the desired $\dot{K}_\theta$ according to (17) until one of the tension bounds is reached. The angular deflection $\delta\theta$ as well as the perturbation torque δT are recorded all along the experiment so that the stiffness $K_\theta = \delta T/\delta\theta$ can be estimated at each sampling time. An estimation of $\dot{K}_\theta$ can then be computed as the slope of a linear interpolation performed on the estimated stiffness K_θ.

Fig. 7 depicts an example of experiment and shows the evolution of the system variables along the time. The configuration is the same all along the experiment while the articular velocities are non-null (see top of Fig. 7). The experiment is here stopped when the tension F_2 reaches the lower tension bound of 4 N (see middle of Fig. 7). The stiffness derivative $\dot{K}_\theta$ is estimated as the slope coefficient a of the linear interpolation on the estimated stiffness evolution along the time t (see bottom of Fig. 7).

The experimental results and their comparison to the simulations are depicted in Fig. 8. The computed slope coefficient in Fig. 7 is represented by the red point in $\theta^* = 1.31$ rad. As in Section 4.3, the maximum variation range is obtained for $\theta^* = \pi/2$ rad in accordance with the model prediction, and this range is shrinking when the system configuration goes toward $\pi/4$ rad. The stiffness derivative modulation capacity of the system using this strategy is here experimentally confirmed and matches correctly the simulations with a mean error of 15% (standard deviation of 8% and maximum of 26%). One can notice that the error is slightly superior to the one in Section 4.3, which can be explained by the more delicate experimental protocol.

5. Discussion

With simple controllers composed of proportional gains, the trajectories along the angular range are tracked with static error below the encoder resolution and mean tracking errors below 9×10^{-2} rad. This result holds even for high dynamics trajectories with respect to the targeted applications. This clearly outlines the intrinsic advantage of tensegrity mechanisms that are composed of low inertia components. The design of the control schemes based on a kinematic modeling of the
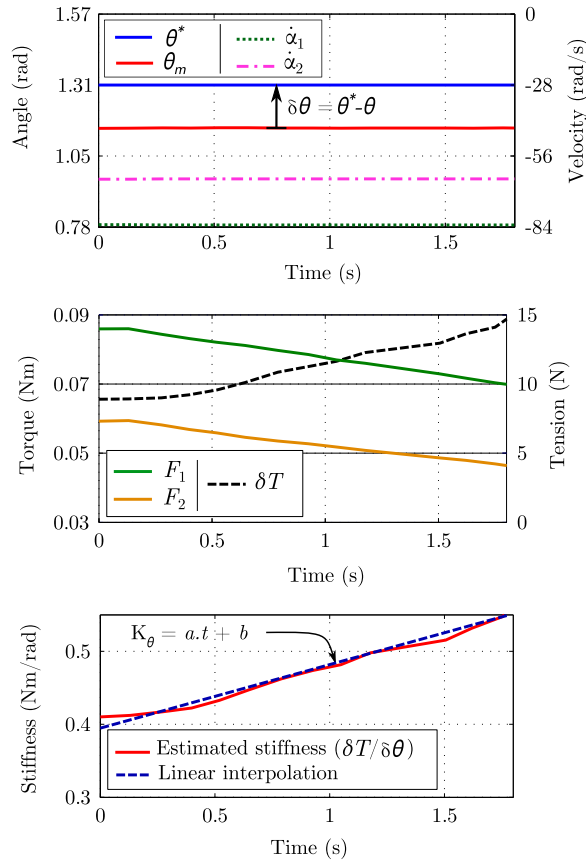
Fig. 7. Example of stiffness derivative modulation experiment: $\theta^* = 1.31$ rad and $\dot{K}_\theta = \dot{K}_\theta^{max}$. (For interpretation of the references to color in this figure caption, the reader is referred to the web version of this paper.)
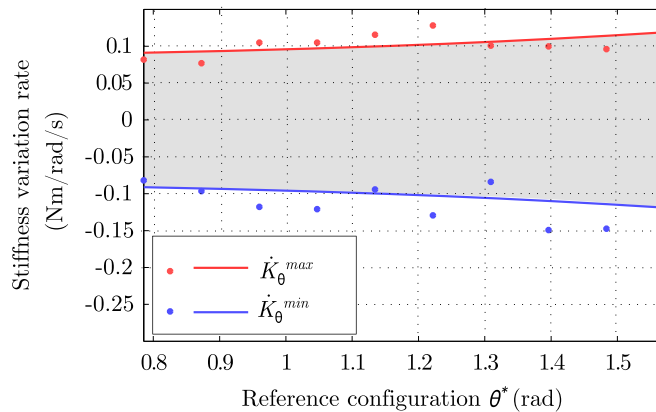

Fig. 8. Modulation of stiffness derivative. The predicted values are in plain lines and the experimental data in points. Gray area represents the theoretical accessible achievable range of stiffness derivative.

system is a relevant approach in this context.

In addition, the considered trajectories are correctly tracked even if errors in the model parameters are introduced. Large variations regarding the usual knowledge of the parameters have no significant impact on the system behavior.

The stiffness of the system is experimentally modified by a significant factor, equal to 3 in the best case, and the whole stiffness range is explored in a few seconds for any configuration thanks to the modulation of the stiffness derivative. Moreover, experiments accurately match the simulation predictions. This means that it is possible to use stiffness model prediction reliably to set a stiffness or a stiffness derivative value.

6. Conclusion

In this paper, two strategies for the control of a planar cable-driven tensegrity mechanism as a variable stiffness device are introduced. They both allow for a reconfiguration of the considered mechanism. The first strategy proposes an original use of the tension distribution algorithm to provide a modulation of stiffness. The second one introduces a novel velocity distribution algorithm and allows for a modulation of stiffness derivative. Both strategies have been experimentally assessed in terms of reconfiguration and stiffness modulation on a dedicated setup, with promising results. We indeed show our ability to modify the passive stiffness of a tensegrity mechanism through a modification of its level of prestress.

Future works will now be focused on the generalization of the control strategies to other tensegrity mechanisms, including spatial ones. Exploitation of the control schemes proposed in this paper should be possible, given the fact that the static model on which the control strategies are built can be obtained in a generic way using form-finding methods [22].

Interesting perspective will be then to compare the performances with those of other variable stiffness devices [11]. Another perspective is the combination of the presented control strategy with an approach such as actuators impedance control to enlarge variations of stiffness.

Acknowledgment

Appendix A.   Derivation of constraints for the velocity distribution algorithm

The bounds of the articular velocities are specified so that the cable tensions do not reach $\mathbf{F_{min}}$ or $\mathbf{F_{max}}$ within a time T, that is at least equal to the sampling time. The spring characteristics are known, so the relationship between the tensions and the cable positions can be exploited.

Considering t_0 as the current time, the first time derivative of $\mathbf{F}$ can be expressed using finite difference between time t_0 and $t_0 + T$ as

$$\dot{\mathbf{F}} = \frac{\mathbf{F}^{t_0+T} - \mathbf{F}^{t_0}}{T} \tag{A.1}$$

and the following inequality on $\dot{\mathbf{F}}$ can therefore be formulated from our initial specifications:

$$\frac{\mathbf{F_{min}} - \mathbf{F}^{t_0}}{T} \leq \dot{\mathbf{F}} \leq \frac{\mathbf{F_{max}} - \mathbf{F}^{t_0}}{T} \tag{A.2}$$

that bounds the tension variation within the time interval $[t_0, t_0 + T]$. Then using the following relationship derived from the springs elastic behavior:

$$\dot{\mathbf{F}} = k(\dot{\mathbf{l}} - \dot{\mathbf{q}}) \tag{A.3}$$

the articular velocities can be bounded accordingly using (A.3) and (A.2) as

$$\dot{\mathbf{l}} + \frac{\mathbf{F}^{t_0} - \mathbf{F_{max}}}{kT} \leq \dot{\mathbf{q}} \leq \dot{\mathbf{l}} + \frac{\mathbf{F}^{t_0} - \mathbf{F_{min}}}{kT} \tag{A.4}$$

where $\mathbf{F}^{t_0}$ can be estimated through the tension measure $\mathbf{F}_m$.

References

[1] R. Motro, Tensegrity: Structural Systems for the Future, Elsevier, London, UK, 2003.
[2] Y. Koizumi, M. Shibata, S. Hirai, Rolling tensegrity driven by pneumatic soft actuators, in: Proceedings of the 2012 IEEE ICRA, Saint Paul, Minnesota, USA, 2012, pp. 1988–1993.
[3] A. Sabelhaus, J. Bruce, K. Caluwaerts, P. Manovi, R. Firoozi, S. Dobi, A. Agogino, V. SunSpiral, System design and locomotion of SUPER ball, an untethered tensegrity robot, in: Proceedings of the 2015 IEEE ICRA, Seattle, WA, USA, 2015, pp. 2867–2873.
[4] J. Friesen, A. Pogue, T. Bewley, M. de Oliveira, R. Skelton, V. SunSpiral, DuCTT: a tensegrity robot for exploring duct systems, in: Proceedings of the 2014 IEEE ICRA, Hong Kong, China, 2014, pp. 4222–4228.
[5] C. Sultan, M. Corless, R.E. Skelton, Tensegrity flight simulator, J. Guid. Control Dyn. 23 (6) (2000) 1055–1064.
[6] J. Aldrich, R. Skelton, K. Kreutz-Delgado, Control synthesis for a class of light and agile robotic tensegrity structures, in: Proceedings of the 2003 IEEE ACC, vol. 6, Denver, Colorado, USA, 2003, pp. 5245–5251.
[7] C. Sultan, R. Skelton, Deployment of tensegrity structures, Int. J. Solids Struct. 40 (18) (2003) 4637–4657.
[8] A.G. Tibert, S. Pellegrino, Deployable tensegrity reflectors for small satellites, J. Spacecr. Rockets 39 (5) (2002) 701–709.
[9] S.D. Guest, The stiffness of tensegrity structures, IMA J. Appl. Math. 76 (1) (2011) 57–66.
[10] M. Azadi, S. Behzadipour, Variable antagonistic stiffness element using tensegrity mechanism, in: Proceedings of the 2007 ASME IMECE2007, Seattle,

WA, USA, 2007, pp. 21–28. http://dx.doi.org/10.1115/IMECE2007-42475.

[11] B. Vanderborght, A. Albu-Schaeffer, A. Bicchi, E. Burdet, D. Caldwell, R. Carloni, M. Catalano, O. Eiberger, W. Friedl, G. Ganesh, M. Garabini, M. Grebenstein, G. Grioli, S. Haddadin, H. Hoppner, A. Jafari, M. Laffranchi, D. Lefeber, F. Petit, S. Stramigioli, N. Tsagarakis, M.V. Damme, R.V. Ham, L. Visser, S. Wolf, Variable impedance actuators: a review, Robot. Auton. Syst. 61 (12) (2013) 1601–1614.

[12] I. Ebert-Uphoff, P. Voglewede, et al., On the connections between cable-driven robots, parallel manipulators and grasping, in: Proceedings of the 2004 IEEE ICRA, vol. 5, IEEE, New Orleans, LA, USA, 2004, pp. 4521–4526.

[13] C. Paul, F.J. Valero-Cuevas, H. Lipson, Design and control of tensegrity robots for locomotion, IEEE Trans. Robotics 22 (5) (2006) 944–957.

[14] Y. Hagiwara, M. Oda, Transformation experiment of a tensegrity structure using wires as actuators, in: Proceedings of the 2010 IEEE ICMA, Xi'an, China, 2010, pp. 985–990.

[15] M. Gouttefarde, J. Lamaury, C. Reichert, T. Bruckmann, A versatile tension distribution algorithm for n-DOF parallel robots driven by $n+2$ cables, IEEE Trans. Robot. 31 (6) (2015) 1444–1457.

[16] R. Bostelman, J. Albus, N. Dagalakis, A. Jacoff, Robocrane project: an advanced concept for large scale manufacturing, in: Proceedings of the 1996 AUVSI, Orlando, FL, USA, 1996, pp. 509–522.

[17] S. Abdelaziz, L. Esteveny, L. Barbé, P. Renaud, B. Bayle, M. de Mathelin, Development of a MR-compatible cable-driven manipulator: design and technological issues, in: Proceedings of the 2012 IEEE ICRA, Saint Paul, MN, USA, 2012, pp. 1488–1494. http://dx.doi.org/10.1109/ICRA.2012.6225302.

[18] R.E. Skelton, J.W. Helton, R. Adhikari, J. Pinaud, W. Chan, An introduction to the mechanics of tensegrity structures, in: The Mechanical Systems Design Handbook, Electrical Engineering Handbook, CRC Press, 2001.

[19] A. Bruyas, F. Geiskopf, L. Meylheuc, P. Renaud, Combining multi-material rapid prototyping and pseudo-rigid body modeling for a new compliant mechanism, in: 2014 IEEE International Conference on Robotics and Automation (ICRA), 2014, pp. 3390–3396.

[20] Q. Boehler, M. Vedrines, S. Abdelaziz, P. Poignet, P. Renaud, Toward an MR-compatible needle holder with adaptive compliance using an active tensegrity mechanism, in: Surgetica 2014, Chambéry, France, 2014.

[21] Q. Boehler, I. Charpentier, M.S. Vedrines, P. Renaud, Definition and computation of tensegrity mechanism workspace, ASME J. Mech. Robot. 7 (4) (2015) 044502-1–044502-4.

[22] M. Arsenault, C.M. Gosselin, Kinematic, static, and dynamic analysis of a planar one-degree-of-freedom tensegrity mechanism, ASME J. Mech. Des. 127 (6) (2005) 1152–1160.

[23] M.A. Khosravi, H.D. Taghirad, Robust PID control of fully-constrained cable driven parallel robots, Mechatronics 24 (2) (2014) 87–97.

[24] S. Bouchard, C. Gosselin, B. Moore, On the ability of a cable-driven robot to generate a prescribed set of wrenches, ASME J. Mech. Robot. 2 (1) (2009) 011010-1–011010-9.

[25] L. Mikelsons, T. Bruckmann, M. Hiller, D. Schramm, A real-time capable force calculation algorithm for redundant tendon-based parallel manipulators, in: Proceedings of the 2008 IEEE ICRA, Pasadena, CA, USA, 2008, pp. 3869–3874. http://dx.doi.org/10.1109/ROBOT.2008.4543805.

[26] Q. Boehler, A. Zompas, S. Abdelaziz, M.S. Vedrines, P. Poignet, P. Renaud, Experiments on a variable stiffness tensegrity mechanism for an MR-compatible needle holder, in: Joint Workshop on New Technologies for Computer/Robot Assisted Surgery (CRAS), Brussels, Belgium, 2015.